

## Organization and Structure of Clouds and Precipitation on the Mid-Atlantic Coast of the United States. Part IV: Retrieval of the Thermodynamic and Cloud Microphysical Structures of a Frontal Rainband from Doppler Radar Data

BART GEERTS AND PETER V. HOBBS

*Atmospheric Sciences Department, University of Washington, Seattle, Washington*

(Manuscript received 11 June 1990, in final form 17 December 1990)

### ABSTRACT

The thermodynamic and cloud structure of a relatively weak wintertime frontal rainband are derived from dual-Doppler radar measurements, soundings and high resolution surface observations, and with a cloud model. These derivations are simplified by the high degree of two-dimensionality and steadiness of the rainband. Water vapor, cloud water, cloud ice, rain, and snow are parameterized in the cloud model, subject to a temperature distribution that is constrained to a dynamical balance. Air temperature is derived from buoyancy, which is retrieved from the airflow assuming momentum and heat balance. The results of the thermodynamic and cloud microphysical retrieval are compared with airborne measurements in the rainband.

The analysis indicates that the rainband was driven by a weak cold front aloft (CFA), which made the prefrontal air conditionally symmetrically unstable. The CFA appeared as a midlevel intrusion of cold, dry air on the meso- $\gamma$  scale. The CFA interacted dynamically with the planetary boundary layer, not only through cooling produced by evaporating hydrometeors but also by a shallow downdraft immediately to the rear of the rainshaft associated with the rainband.

This study shows that the combined thermodynamic and cloud microphysical retrieval technique is a useful tool in analyzing force balances and assessing water and energy budgets, even in quite weak mesoscale precipitation systems.

### 1. Introduction

In the first part of this series (Locatelli et al. 1989, hereafter referred to as Part I) we described the evolution of the large-scale frontal structure of a cyclone as it moved eastward across the United States from 4 to 7 March 1986. The further development of the cyclone along the east coast of the United States and Canada from 7 to 8 March 1986 has been described by Yau and Jean (1989). The evolution of this system over the Mid-Atlantic States was well documented as part of the Genesis of Atlantic Lows Experiment (GALE 1985). In Part I, the formation of two rainbands ahead of a cold front aloft (CFA) was explained in a synoptic context. These rainbands, in particular the second one, were examined in more detail by Sienkiewicz et al. hereafter referred to as Part II, (1989). In the present paper, the dynamical structure of the second rainband, referred to as R2, is examined with the aid of a 3 h sequence of dual-Doppler radar data, as well as surface and airborne measurements. The air motion field is related to the dynamics of the rainband using a model, which we will call "combined thermodynamic and microphysical retrieval" (combined

TMR). This model relates thermodynamic and cloud microphysical variables to an input airflow field, and to each other, in a self-consistent way.

The term "thermodynamic retrieval" is used to indicate the diagnostic derivation of pressure and buoyancy fields that are in equilibrium with an input airflow field and specified or floating boundary conditions (e.g., Gal-Chen 1978; Hane and Scott 1978). The method has been applied previously to storms with strong updrafts, including squall lines (Roux et al. 1984; Lin et al. 1986), tornado-spawning storms (Brandes 1984; Hane and Ray 1985), a strong cold-frontal rainband (Parsons et al. 1987), as well as to a planetary boundary layer (PBL) inversion (Gal-Chen and Kropfli 1984). Two approaches have been used: a purely dynamic approach, which employs only momentum conservation constraints (e.g., Gal-Chen 1978; Brandes 1984; Matejka 1989), and a thermodynamic approach, which also uses the first law of thermodynamics (e.g., Roux 1988). The inclusion of the first law requires an accurate estimate of the distribution of heating.

"Microphysical retrieval" refers to the diagnostic derivation of the distribution of clouds, hydrometeors and temperature in equilibrium with a given airflow field, using a cloud microphysical model. Momentum conservation constraints are ignored. Either a parameterized or an explicit cloud model may be used (e.g., Lin et al. 1983; Rutledge and Hobbs 1983; Ziegler 1985;

---

Corresponding author address: Dr. Peter V. Hobbs, Dept. of Atmos Science, AK-40, University of Washington, Seattle, WA 98195.

Hauser and Amayenc 1986; Chong and Hauser 1989; Le Cam and Isaka 1989).

Thermodynamic and microphysical retrieval need not be independent. Microphysical retrieval supplies an estimate of latent heating, which can be used in thermodynamic retrieval to calculate buoyancy, which in turn affects temperature, saturation mixing ratio and the distribution of cloud and hydrometeors. Hauser et al. (1988) used a model of combined TMR to study a tropical squall line, but their microphysical parameterization was very simplified. Their technique was applied to a narrow cold-frontal rainband by Roux and Hauser (1989).

In the present paper, a parameterized cloud microphysical model has been combined with a model of thermodynamic retrieval, based on Hauser et al. (1988), to investigate the weakly convective rainband R2. Because of the high degree of along-band homogeneity of R2 during the period of our analysis, the model used is two-dimensional. Both thermodynamic and microphysical retrieval generally assume the airflow field to be stationary, although this is not a necessary condition provided that changes in the airflow field are documented (Matejka 1989). However, the inclusion of time adds another source of error in the processing of data from ground-based Doppler radars, especially in a rapidly moving system. In the case of R2, both two-dimensionality and steady state—intriguing physical characteristics in their own right—are demonstrated by the high consistency of the derived circulation pattern in a storm-relative cross section over a period of 1 h, during which time R2 moved through the area covered by the dual-Doppler radars. However, the maximum vertical velocities in this rainband were only  $\sim 1.6 \text{ m s}^{-1}$ . To our knowledge, this is the first time that thermodynamic retrieval, and combined TMR, have been applied to such a weak system. It is also the first time that TMR results have been verified against independent in situ measurements.

In the next section, we describe briefly the derivation of the airflow field from the dual-Doppler radar data. An outline of the TMR method is given in section 3. The results of the application of the TMR model to rainband R2 are presented in section 4, with the analyses in Part I and Part II as background.

## 2. The input flow field

All retrievals are based on a 2-D ( $x, z$ ), storm-relative airflow field on a Cartesian grid. The advection speed of the frame of reference (the “storm motion”) is chosen to minimize changes in the radar reflectivity field between consecutive radar volumes (Gal-Chen 1982). This storm motion, defined to be independent of height, is close to the velocity of the precipitation cores derived from radar observations (see Table 1 in Part II). The airflow is based on 3-D gridded data obtained from two 5.5 cm wavelength ground-based radars (the

NCAR CP-3 and CP-4 radars), which were scanned conically in a dual-Doppler mode. The radial velocities were synthesized on a Cartesian grid moving with the storm. The velocity data were filtered to a threshold wavelength of 4 km, which is comparable to the resolution of the conical radar scans.

The vertical air velocity ( $w$ ) was obtained by integrating the anelastic continuity equation vertically. Surface observations of convergence (from the GALE PAM II network data) were used to derive the convergence field at the surface at locations where the lowest radar beam was above half the vertical grid spacing (250 m); the convergence calculated from surface observations was given the same weight as the convergence derived from the lowest radar scan at other locations. The continuity equation was integrated upward, with zero vertical velocity at the ground. To dampen the errors in  $w$  at the top of the rainband, a second boundary condition was imposed by modifying the horizontal convergence mainly at the higher levels without adjusting the horizontal velocity field (O'Brien 1970). Because the cloud top was higher than the highest level of the grid (8 km versus 7 km), the top boundary condition for  $w$  was assumed to be proportional to the local radar reflectivity, with a maximum  $w$  of  $0.25 \text{ m s}^{-1}$  at  $x = 20 \text{ km}$  and a minimum of zero at  $x = 50 \text{ km}$ . These values were chosen so that the average  $w$  at the top did not change with the addition of the second boundary condition. This integration method seemed to yield the most reasonable distribution of  $w$ , even though the accuracy of  $w$  for this integration method decreases with height.

Averaging over a distance of 26 km along the length of R2 reduced the airflow field to two dimensions. The mean along-band convergence was computed to be only 16% of the mean across-band convergence in the averaging domain. Therefore, the 2-D flow is close to anelastic mass balance (Hauser and Amayenc 1986). There was some variation of  $w$  in the 26 different sections that were averaged together (the average standard deviation of  $w$  in the along-direction was  $0.18 \text{ m s}^{-1}$ , with a standard deviation of  $0.15 \text{ m s}^{-1}$ , and a maximum of  $0.53 \text{ m s}^{-1}$ ), but the general pattern was the same in all.

Both the integration method and the 2-D reduction violated the mass continuity equation. Over the entire cross section, there was a net influx of air, but, measured as a fraction of the integrated absolute convergences, the integrated mass imbalance was small (6.8%). Also, the effect of mass imbalance on the retrieval results was small.

## 3. The method of combined retrieval

### a. The basic equations

Let  $x$  and  $y$  be the across-band and along-band storm-relative coordinates, respectively,  $u$  and  $v$  the corresponding horizontal storm-relative air motions,

and  $U$  and  $V$  the corresponding components of storm motion. Then  $x = X - Ut$  and  $y = Y - Vt$ , where  $X$  and  $Y$  are the coordinates in the ground-relative frame of reference and  $t$  is time. A storm-relative frame of reference is chosen to minimize the effect of advection in the tendency terms in the equations of motion and water continuity equations. An accurate estimate of the advection is particularly important for rainbands, which may maintain their integrity for a long time in an environment of strong advection and weak vertical motions.

Since the air motion is prescribed and assumed to be in steady state, linearization of all terms in the momentum conservation equations in the horizontal and vertical yields:

$$u \frac{\partial u}{\partial x} + w \frac{\partial u}{\partial z} = -\theta_{vb} \frac{\partial \pi'}{\partial x} + f(v + V) - f'w + F_1 \quad (1)$$

$$u \frac{\partial w}{\partial x} + w \frac{\partial w}{\partial z} = -\theta_{vb} \frac{\partial \pi'}{\partial z} + f'(u + U) + gB_\pi + F_3 \quad (2)$$

where,  $w$  is the vertical air velocity,  $z$  the vertical coordinate,  $g$  the gravitational acceleration,  $f$  the Coriolis parameter and  $f'$  its derivative with respect to latitude,  $\pi \equiv T(c_p/\theta)$ , and  $\theta \equiv T(p_0/p)^k$  is the potential temperature where  $k \equiv (R_d/c_p)$  and  $c_p$  is the specific heat of dry air at constant pressure and  $R_d$  the gas constant for dry air. The temperature is denoted by  $T$ , the pressure by  $p$ , the density by  $\rho$ , and  $p_0 = 1000$  mb;  $\theta_v = \theta(1 + 0.61q_v)$  is the virtual potential temperature, and  $q_v$  the specific humidity. The subscript  $b$  in  $\theta_{vb}$  (and in other variables) refers to a basic state. The buoyancy is defined as

$$B_\pi = \frac{\theta'}{\theta_b} + 0.61q'_v - q_t = \frac{\theta'}{\theta_b} + \xi \quad (3)$$

where,  $\xi \equiv 0.61q'_v - q_t$ . The total liquid and solid water mixing ratio ( $q_t$ ), in kilogram per kilogram of moist air, is the sum of the rain ( $q_r$ ), snow ( $q_s$ ), cloud water ( $q_c$ ) and cloud ice ( $q_i$ ) mixing ratios. The buoyancy defined by (3) is simpler than the commonly used relative density perturbation  $B_\rho$ :

$$B_\rho \equiv -\frac{\rho'}{\rho_b} = -\frac{c_v \pi'}{R_d \pi_b} + \frac{\theta'}{\theta_b} + \xi = -\frac{c_v \pi'}{R_d \pi_b} + B_\pi \quad (4)$$

where,  $c_v$  is the specific heat of dry air at constant volume. The buoyancy  $B_\pi$ , used in combination with the variables  $\pi$  and  $\theta$ , is unaffected by the Exner pressure  $\pi$ . In (1) and (2)  $F_1$  and  $F_3$  represent the parameterization of subgrid-scale mixing. The diffusivity is assumed to be a function of the deformation field (Smagorinski 1963). The Coriolis force is included in (1) and (2) because of the rapid storm movement and because the width of the cross section, which encompasses the essential parts of the circulation of R2, is quite large (60 km) compared to the horizontal dimension

in 3-D retrievals (e.g., Parsons et al. 1987; Lin et al. 1986).

Some important assumptions adopted in the above equations, in particular the linearization in (1)–(2), are related to the separability of  $\pi$ ,  $\theta$  and  $q_v$  into a basic state and a much smaller perturbed state (indicated by a prime), for example  $\psi = \psi'(x, z, t) + \psi_b(z)$ . The most important assumption is that, as a consequence of the linearization of the vertical momentum conservation equation (2):

$$\frac{d\pi_b}{dz} = -\frac{g}{\theta_{vb}} \quad (5)$$

In other words, the basic state is hydrostatically balanced.

Equations (1) and (2) can be written as

$$\frac{\partial \pi'}{\partial x} = \Phi \quad (6)$$

$$\frac{\partial \pi'}{\partial z} = g \frac{B_\pi}{\theta_{vb}} + \Gamma \quad (7)$$

where  $\Phi$  and  $\Gamma$  contain all the terms in (1) and (2) that depend only on the input air velocity. This way, known and unknown terms are separated. The pressure perturbation is hydrostatically balanced if the pressure perturbation gradient force exactly cancels the buoyancy force. Assuming steady state, the first law of thermodynamics, when linearized in the unknowns, can be written as

$$u \frac{\partial \theta'}{\partial x} + w \frac{\partial \theta'}{\partial z} = -w \frac{\partial \theta_b}{\partial z} + \frac{\Lambda}{\pi_b} + F_\theta \quad (8)$$

where  $F_\theta$  is the subgrid-scale heat mixing rate, computed as in Ziegler (1984), and  $\Lambda$  is the latent heating (in  $\text{W kg}^{-1}$ ), which is calculated from parameterized microphysical interactions.

### b. Microphysical parameterizations

The bulk cloud microphysical model is based on Rutledge and Hobbs (1983). Five constituents are considered: water vapor ( $q_{vb} + q'_v$ ), rain ( $q_r$ ), cloud water ( $q_c$ ), snow ( $q_s$ ) and cloud ice ( $q_i$ ). Graupel is ignored, because aircraft observations indicated that if it was present at all in R2 it was in negligible amounts, except perhaps in the cumulus clouds to the rear of R2 (see Fig. 9a in Part II). Also, a third variable for the ice phase does not seem to add much freedom to the bulk parameterization (Chong and Hauser 1989; Rutledge and Hobbs 1984).

In the bulk parameterization, the size distribution of cloud ice is assumed to be monodispersed. The snow and rain are assumed to follow a Marshall–Palmer distribution, which has two parameters, one of which (the slope) is derived from the local mass of rain and snow, and the other (the intercept) is a constant [ $8 \times 10^6$

$m^{-4}$ , for a weakly convective narrow cold-frontal rainband (Rutledge and Hobbs 1984)]. The cloud water is distributed according to the two-parameter Khrgian-Mazin droplet size distribution (Pruppacher and Klett 1978), with one parameter specified from  $q_c$  and the other, the total droplet number concentration, a constant (here  $3 \times 10^8 m^{-3}$ ) derived from aircraft observations. The collision and coalescence efficiencies are computed for all rain drop and cloud droplet sizes based on data from Beard and Ochs (1984).

The water continuity equation for cloud ice ( $q_i$ ) is replaced with the one for total liquid and frozen water ( $q_l$ ), because the equation for the latter is much simpler (the only source/sink terms are the interaction with water vapor and the fallout of precipitation). Thus, the water continuity equations may be written as

$$u \frac{\partial q_l}{\partial x} + w \frac{\partial q_l}{\partial z} = E_{23} + E_{13} + \frac{\partial}{\partial z} (\rho q_r V_{t,rain} + \rho q_s V_{t,snow}) + F_l \quad (9)$$

$$u \frac{\partial q'_v}{\partial x} + w \frac{\partial q'_v}{\partial z} = -E_{23} - E_{13} - w \frac{dq_{vb}}{dz} + F_v \quad (10)$$

$$u \frac{\partial q}{\partial x} + w \frac{\partial q}{\partial z} = S + F + \frac{\partial}{\partial z} (\rho q V_t) \quad (11)$$

where,  $V_t$  is the terminal fallspeed,  $\Lambda = L_{23}E_{23} + L_{13}E_{13} + L_{12}E_{12}$ ,  $L_{ij}(T)$  the latent heat (in  $J kg^{-1}$ ) between phase  $j$  and phase  $i$ , and  $E_{ij}$  the flux (in  $kg kg^{-1} s^{-1}$ ) from phase  $j$  to phase  $i$  ( $1 \equiv$  solid,  $2 \equiv$  liquid,  $3 \equiv$  gas).  $F_l$ ,  $F_v$  and  $F$  are the subgrid-scale mass mixing rates for the various constituents, computed as described by Ziegler (1984). The terms  $V_{t,rain}$  and  $V_{t,snow}$  are the terminal velocities of rain and snow, respectively. The term  $S$  includes all nondiffusive sources.

Equation (11) is a general expression, applicable to rain, snow and cloud water. The sources/sinks of cloud water ( $q_c$ ) include water vapor condensation, melting of ice, conversion of cloud water to rain, and accretion on rain drops or snow. In addition to autoconversion and accretion of cloud droplets, the sources/sinks of rain ( $q_r$ ) include water vapor condensation and melting of snow. Snow ( $q_s$ ) is affected by deposition, melting, autoconversion and accretion of ice.

A schematic of the water classes and parameterized interactions is shown in Fig. 1. The local sources/sinks of water by horizontal or vertical advection are not shown in this figure. Most source/sink terms on the right hand side of Eqs. (9)–(11) are calculated as in Rutledge and Hobbs (1983). Notable exceptions include ice initiation and accretion (see Geerts 1990).

### c. Solution procedures

#### 1) MICROPHYSICS

Equations (9)–(11) can be written in the general form:

$$u \frac{\partial Q}{\partial x} + w \frac{\partial Q}{\partial z} = \Psi \quad (12)$$

where,  $Q$  is any water variable (in this case  $q_r$ ,  $q_s$ ,  $q_c$ ,  $q_i$ , and  $q'_v$ ), and  $\Psi$  corresponds to the respective expression on the right-hand side of (9)–(11);  $\Psi$  consists of nonlinear functions of the water species, especially  $q'_v$ .

Equation (12) is solved as an initial value problem. Because certain parameterizations are dependent on a time step (e.g., condensation, melting, initiation of cloud ice), we can speak of an iteration *time* rather than the *number* of iterations. From the perspective of an initial value problem, a parcel of air traveling at a given speed moves a fixed distance along its trajectory. The initial guess for the fields of thermodynamic and microphysical variables is based on an upstream and a downstream sounding, an array of surface observations (e.g., a high frequency mesonet observations with time converted to space), as well as radar reflectivity and vertical air velocity data. Inflow across the boundaries, as well as the relative humidity (RH) at the surface, are fixed through the choice of the initial fields. Interior grid points and the top boundary (where  $w$  is close to zero), as well as outflow boundaries, vary and eventually reach an equilibrium solution, at which time (12) is satisfied. An upwind advection scheme is used, with the upwind displacement determined by the timestep and the local windspeed. The advection gradients are calculated on an interpolated surface (bicubic spline). Since this scheme is not strictly conservatory, the water budget has to be evaluated during the solution procedure.

#### 2) BUOYANCY

Combining (3) with (8):

$$u \frac{\partial B_\pi}{\partial x} + w \frac{\partial B_\pi}{\partial z} = \Omega \quad (13)$$

where

$$\Omega \equiv - \left( 1 + \frac{\theta'}{\theta_b} \right) w \frac{d\theta_b}{dz} \frac{1}{\theta_b} + \frac{\Lambda}{(\pi_b \theta_b)} + \frac{F_\theta}{\theta_b} + u \frac{\partial \xi}{\partial x} + w \frac{\partial \xi}{\partial z}$$

and  $\xi$  is defined by Eq. (3). Equation (13) is still the first law of thermodynamics, an advection-type equation of the same form as (12), and it can be solved using the same method. Here, a variational solution is sought not only for  $\pi'$ , as is generally done in thermodynamic retrieval (e.g., Gal-Chen 1978), but also for the buoyancy  $B_\pi$ , in order to optimally satisfy both (13) and vertical momentum conservation [Eq. (2)] (Hauser et al. 1988).

To evaluate  $B_\pi$ , we use both thermodynamic [Eq. (13)] and dynamic [eqns. (1) and (2)] information. To do so, we proceed in the same manner as Hauser et al. (1988). From  $\partial(\text{Eq}(6))/\partial z - \partial(\text{Eq}(7))/\partial x$ :

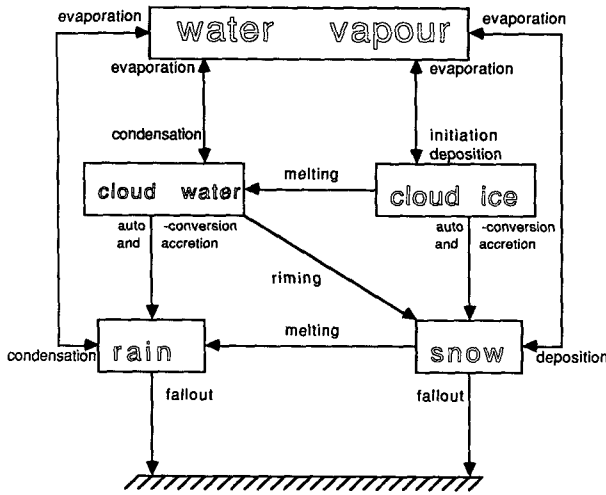


FIG. 1. Schematic of the cloud microphysical classes and exchange processes included in the cloud microphysics model.

$$\frac{\partial B_\pi}{\partial x} = \frac{\theta_{vb}}{g} \left( \frac{\partial \Phi}{\partial z} - \frac{\partial \Gamma}{\partial x} \right) \equiv \frac{\Theta}{u}. \quad (14)$$

From (13) and (14):

$$w \frac{\partial B_\pi}{\partial z} = \Omega - \Theta. \quad (15)$$

An optimal combination of (14) and (15) requires minimization of

$$\iint \left\{ \left( \frac{\partial B_\pi}{\partial x} - \frac{\Theta}{u} \right)^2 + \frac{1}{V_e^2} \times \left( w \frac{\partial B_\pi}{\partial z} + \Theta - \Omega \right)^2 \right\} dx dz. \quad (16)$$

The functional relation (16) employs the weak constraint formalism of the calculus of variations. According to this formalism, the first squared term is minimized in a global sense subject to the constraint that the second squared term is made as small as desired, depending on the magnitude of the parameter  $V_e$  in (16), which has the dimensions of velocity. The first term in (16) relates the retrieved buoyancy to the momentum equations; the second term in (16) relates the retrieved buoyancy to the first law of thermodynamics. Here  $V_e$  is chosen to be large ( $V_e = 15 \text{ m s}^{-1}$ ) compared to the average storm-relative velocity ( $4.5 \text{ m s}^{-1}$ ), because the first squared term in (16) seems to yield a more accurate buoyancy distribution than the second and because it improved the internal consistency of the equations of motion. Because the relative error for vertical velocity ( $w$ ) is large, much larger than that for  $u$ , the second part of the integral (16) may yield a poor estimate of the vertical distribution of the buoyancy. In fact, a large vertical buoyancy gradient can be erroneously retrieved from a weak vertical velocity field of the wrong sign. Therefore, we anticipate the first term in the integral to be more accurate. The above technique is probably less accurate for stratiform precipitation, where the distribution of updrafts and downdrafts deduced from dual-Doppler radar measurements is less reliable. This affects both the vertical momentum equation and the first law.

Minimization of (16) is a standard problem in the calculus of variations. The buoyancy that minimizes (16) satisfies the Euler equation:

$$V_e^2 \frac{\partial^2 B_\pi}{\partial x^2} + w^2 \frac{\partial^2 B_\pi}{\partial z^2} + \frac{\partial w^2}{\partial z} \frac{\partial B_\pi}{\partial z} = - \frac{\partial(w\Theta)}{\partial z} + V_e^2 \frac{\partial(\Theta/u)}{\partial x} + \frac{\partial(w\Omega)}{\partial z}. \quad (17)$$

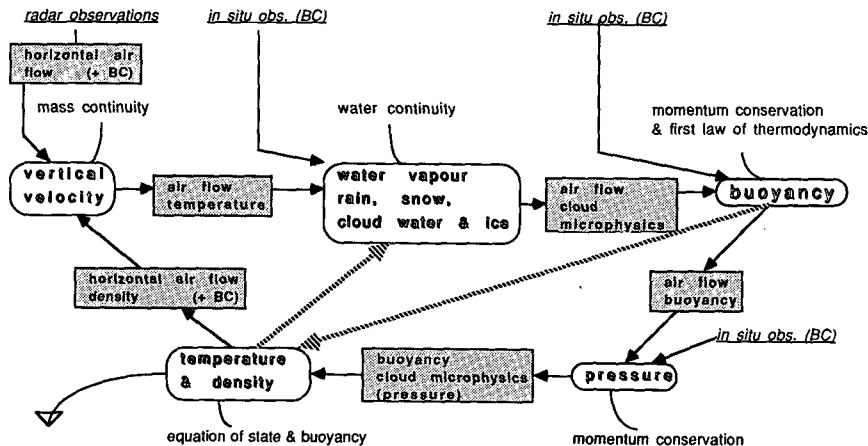


FIG. 2. Flow chart illustrating the combined thermodynamic and microphysical retrieval scheme. The input fields are in the shaded rectangular boxes, the computed fields are in the unshaded rounded boxes. Physical laws and observational data (underlined) used in the retrieval are shown outside of the boxes. The arrows between the boxes indicate the sequence of operations. Shortcuts are possible along the two dotted lines. "BC" stands for boundary conditions.

Because  $V_e^2 > 0$ ,  $w^2 > 0$ , therefore, (17) is elliptic; with proper boundary conditions it can be solved using standard iterative techniques. At the lateral boundaries, the buoyancy is specified from sounding data, as well as radar reflectivity and aircraft data. Because buoyancy is a perturbation variable [see (3)], a reference state has to be defined. Since the 5.5-cm Doppler radars did not provide information on the airflow surrounding the rainband, we arbitrarily chose the leading boundary to constitute the reference state. The buoyancy at the trailing boundary is then determined as the difference between the two soundings. Surface observations were used for the lower boundary. The only requirement at the upper boundary is that the buoyancy be constant with height.

### 3) PRESSURE

Because the horizontal pressure gradient necessary to maintain the horizontal winds in steady state is not always compatible with the vertical pressure gradient necessary to maintain the derived vertical velocity  $w$ , a perturbation pressure  $\pi'(x, z)$  must be found that optimally satisfies (1) and (2) simultaneously; in other words, a distribution of  $\pi'(x, z)$  must be found that minimizes:

$$\iint \left\{ \left( \frac{\partial \pi'}{\partial x} - \Phi \right)^2 + \left( \frac{\partial \pi'}{\partial z} - \frac{gB_\pi}{\theta_{vb}} - \Gamma \right)^2 \right\} dx dz. \quad (18)$$

In contrast with (16), no weighting factor is used in (18). This integral is less sensitive to errors in vertical velocity, but the accuracy of the retrieved pressure is affected by the quality of the buoyancy retrieval. The field of  $\pi'$  that minimizes (18) satisfies the Euler equation:

$$\frac{\partial^2 \pi'}{\partial x^2} + \frac{\partial^2 \pi'}{\partial z^2} = \frac{\partial \Phi}{\partial x} + \frac{g}{\theta_{vb}} \frac{\partial B_\pi}{\partial z} - \frac{gB_\pi}{\theta_{vb}^2} \frac{d\theta_{vb}^2}{dz} + \frac{\partial \Gamma}{\partial z}. \quad (19)$$

Equation (19), which is a Poisson equation, can be solved, with proper boundary conditions, using the same technique as for (17), provided the buoyancy field is known [ $\Phi$  and  $\Gamma$  depend only on the input ( $u$ ,  $v$ ,  $w$ )]. At one lateral boundary, the pressure perturbation is arbitrarily set to zero, and at the other lateral boundary pressure is determined from geostrophic balance of the along-band wind. Surface observations (time converted to space) are used for the lower boundary. As in the case of buoyancy, pressure perturbation is set to be constant with height at the top boundary. Equation (19) is simpler than (17), because in (17) the linear operator, which is more complex than the Laplacian of (19), may not be very accurate.

#### d. Combined retrieval: an iterative solution

Equation (17) can only be solved for  $B_\pi$  if  $q_t$ ,  $q'_v$  and the latent heating  $\Lambda$  are known. Also, the solution of

(19) (for  $\pi'$ ) requires an estimate of  $B_\pi$ . In other words, because the microphysical fields are essential to compute the latent heating, and hence the buoyancy, and since pressure retrieval requires a knowledge of buoyancy, the water variables are solved first, then buoyancy, and finally pressure. A flow chart is shown in Fig. 2. Part of the buoyancy is due to excess temperature which, mainly through the dependence of saturation vapor pressure on temperature, affects the microphysical processes and hence the distribution of water. An accurate estimate of this temperature excess depends on a knowledge of the water distribution (for example, in terms of its effect on buoyancy, a  $3 \text{ g kg}^{-1}$  water loading is equivalent to  $1^\circ\text{C}$  cooling). Because of the strong coupling between buoyancy and microphysics, an iterative solution is required (Fig. 2).

The couplings between pressure and the water variables, and between pressure and buoyancy, are both weak compared to the coupling between the buoyancy and the water variables (Fig. 2). This is because the effect of pressure on the saturation mixing ratio is small compared to the effect of temperature and also because the pressure term in the buoyancy [see (3)] is generally much smaller than the temperature term ( $1^\circ\text{C}$  temperature perturbation corresponds to a 13 mb excess pressure!). Hence, (12) and (17) could be solved many times until they converge, without considering the pressure perturbation in the derivation of temperature from buoyancy. After having obtained an equilibrium solution for buoyancy (and microphysics), (19) could be solved once only. We have not followed this shortcut procedure because the computing time needed to derive pressure is only a fraction of the time needed to solve (12). Ultimately, since air density is updated in every iteration, the vertical velocity could be recomputed by integrating the exact form of the continuity equation (Fig. 2). This sidestep is obviously redundant, given the potentially large errors in the input horizontal airflow and the boundary conditions.

Because the solution of (12) is so computationally intensive, the water variables are actually never solved to equilibrium before buoyancy (and pressure) are calculated. At regular intervals, during the iteration for the water variables, thermodynamic fields in equilibrium with the flow field and the latent heating and water distribution are calculated, and the new temperature field is used in the subcycling for the hydrometeors and water vapor. Water vapor is calculated first in each step of the microphysical iteration, because all other water classes respond rapidly to its presence.

## 4. Application to rainband R2

### a. The mesoscale structure of rainband R2

The location of the field study and the data sources are described in Part II. We now describe briefly some aspects of the mesoscale structure of R2 that are germane to the TMR.

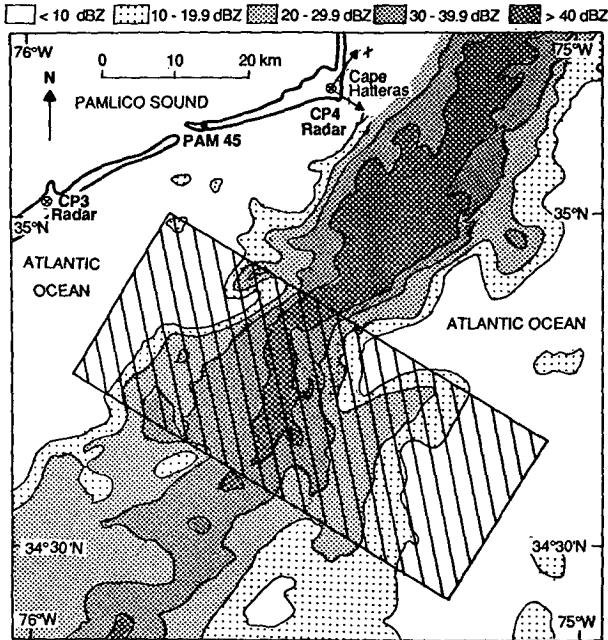


FIG. 3. Radar reflectivity of rainband R2 at an altitude of 1.6 km measured by the CP-4 radar at 2035 UTC 6 March 1986. Increasing intensities of shading correspond to increasing values of the reflectivity as indicated in the key. The location of the CP-3 and CP-4 Doppler radars and the PAM-II surface mesonet station 45 are indicated. The thick contour line is the coastline. Three-dimensional air velocities derived from the Doppler radars were contracted into a cross section across R2 within the hatched area.

Figure 3 shows a section of R2 (which was at least 600 km long) with respect to the most important data sources used in this study. With only little sinuosity and a few convective cells at both sides of R2, the rainband appears to have been quite homogeneous along its length. The apparent widening of R2 toward the SW is due mainly to the broadening of the radar beam and the presence of a melting band just above the lowest PPI.

At 1800 UTC, the rawinsonde station Morehead City (MRH, shown on Fig. 1 in Part II) was situated just ahead of R2 (see Fig. 2 in Part II). Therefore, the 1800 UTC MRH sounding serves as an excellent eastern boundary to the model domain (i.e., the hatched region in Fig. 3), even though in a storm-relative frame it is located about 150 km farther north along R2 than the TMR domain. A representative eastern boundary is important, because at most elevations it is an upstream boundary. The 1800 UTC MRH sounding (Fig. 4a) shows that the planetary boundary layer (PBL), as well as the middle and upper troposphere, were fairly dry; the temperature profile was close to neutral to potential instability. During the passage of R2 between 1800 and 2100 UTC, the temperature dropped only slightly at all levels, up to 1.5°C. However, the specific humidity was redistributed after the passage of R2, with considerable drying of the midtroposphere and some mois-

tening around 900 mb (Fig. 4a). The 2100 UTC MRH sounding, at ~50 km behind R2 and ~100 km south of the model domain, is the best sounding available for the western boundary, which is only an inflow boundary at mid levels. As shown in Fig. 4b, considerable shear existed ahead of as well as behind R2, especially in the lower troposphere. The shear was about 20° more zonal than the alignment of R2, which was oriented essentially parallel to the surface front located 225 km to the rear of R2 (see Fig. 2 in Part II).

### b. Airflow and radar reflectivity

A cross section of the 2-D vector winds is shown in Fig. 5. Isotach analysis indicates a moderate (up to 9 m s<sup>-1</sup>) front-to-rear inflow at all levels, mainly at 1 to 3 km height, and a weaker (up to 5 m s<sup>-1</sup>) rear-to-front inflow between 3 and 4.5 km height. At upper levels, the air ahead of R2 moved at almost the same speed as R2, whereas in the PBL the air flows from front-to-rear under R2. The radar reflectivity contours (Fig. 5) are closed around the maximum reflectivity to the front of R2, and a long anvil is present beyond the rear boundary, as confirmed by aerial photography (see Fig. 10b in Part II).

The vertical velocity in R2, derived from the dual-Doppler radar data, is contoured in Fig. 6. In most areas, the vertical velocity is upward, with two distinct maxima:  $w = 1.6$  m s<sup>-1</sup> at coordinates (33, 4) and  $w = 1.1$  m s<sup>-1</sup> at coordinates (12, 4). The former and stronger maximum is also deeper while the latter maximum, located just above the area of maximum radar reflectivity, is shallower and higher. The area of maximum reflectivity is associated with a downdraft of up to 0.9 m s<sup>-1</sup>. Heavy downpours are often associated with downdrafts. In this case however the spatial coincidence is somewhat surprising, because the downdraft is not shallow; one wonders how much precipitation would have been required to reach the ground through the downdraft. The airflow in other cross sections of R2 have been described previously (e.g., Fig. 2 in Hegg et al. 1989 shows a cross section farther north, and Fig. 8 in Part II shows an along-band average over a larger domain of R2). The similarities of these sections demonstrate the two-dimensional and steady-state nature of R2.

### c. Model results

In this section we present some of the results of the combined TMR model applied to R2 using the airflow and boundary conditions specified in sections 4a and 4b.

#### 1) CLOUD MICROPHYSICS

Figures 7–9 show the distribution of the retrieved cloud microphysical variables, based on a 2 h run of

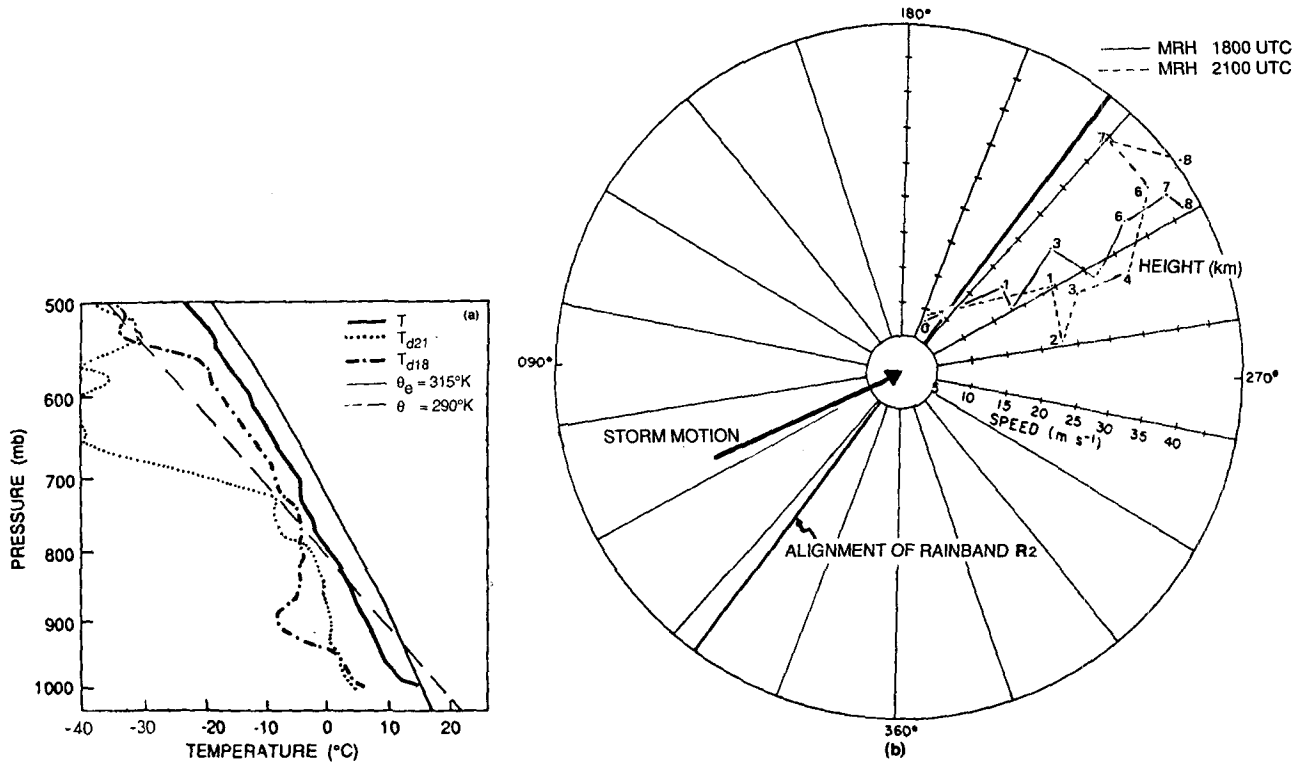


FIG. 4. (a) Sounding from the Morehead City radiosonde released at 1800 UTC 6 March 1986. The moist adiabat for an equivalent potential temperature ( $\theta_e$ ) of 315 K and the dry adiabat for a potential temperature ( $\theta$ ) of 290 K are shown. Also shown are the temperature ( $T$ ) and dewpoint temperature ( $T_{d18}$ ) for the MRH sounding at 1800 UTC, and the dewpoint temperature  $T_{d21}$  for the MRH sounding at 2100 UTC. (b) Hodograph for the MRH soundings at 1800 UTC and 2100 UTC on March 6 1986. Also shown are the alignment of rainband R2 and the storm motion.

the TMR model. Few changes occurred after 2 h (up to 15% or 0.1 g kg<sup>-1</sup>/h, whichever is smaller), which is not surprising since the advective time scale is 2 h

at most and other time scales (sedimentation, initiation. . .) are smaller. Therefore, we can consider the results shown here as quasi-equilibrium. The TMR

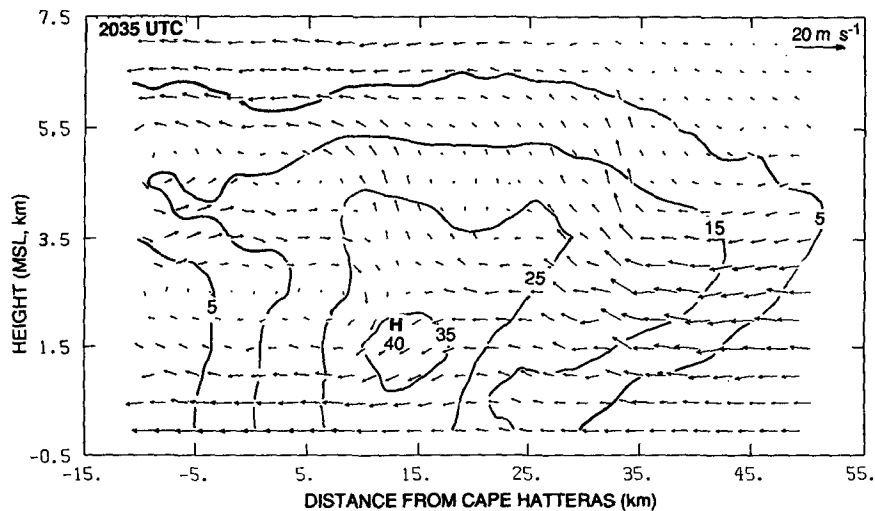


FIG. 5. Vertical cross section across the width of R2 (within the hatched rectangle shown in Fig. 3) of the airflow (in a storm-relative frame of reference) derived from the Doppler radars at 2035 UTC March 6 1986. The radar reflectivity field is contoured in dBZ units. The symbol "H" is used here (and in the following figures) to indicate local maxima.

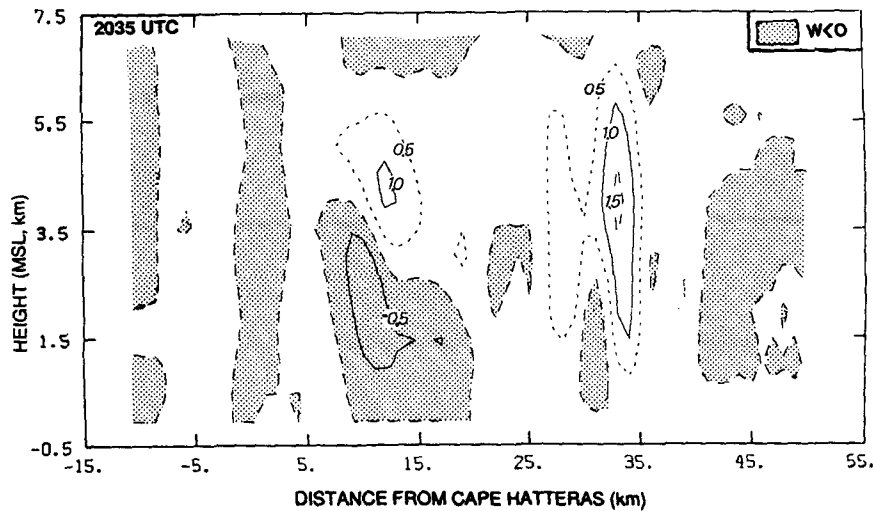


FIG. 6. As for Fig. 5 but for vertical velocity (in  $\text{m s}^{-1}$ ) field. Negative values are shaded.

model develops a large amount of snow (Fig. 7b), especially in and downstream of areas with updrafts close to the fallspeed of snow. In these areas of the model, snow grew mainly by deposition in an area that was saturated with respect to ice (Figs. 8 and 9), and rain was formed mainly through the melting of snow (Fig. 7a). Some rain is also shown close to the rear boundary

at 1 to 2 km in height; it is mainly produced by collection. The moistening of the lower troposphere by the passage of R2 is in accordance with measurements (Fig. 4a; Fig. 7 in Part II; and Fig. 15 in Part I, in particular between MRH 2020 UTC and MRH 1710 UTC). The evaporation of rain falling from R2 is also seen in the reflectivity trace of the UW 35 GHz vertically-pointing radar (see Fig. 7 in Part II) and in aerial photography. In particular, the latter two sources confirm the presence of shallow precipitating cumulus to the rear of R2, of the kind predicted by the model at the same location (Fig. 7).

Cloud ice (Fig. 8) is present in the updrafts (Fig. 6) and it is also more prevalent in areas with high cloud water concentration (Fig. 8); this is due to the dependence of ice initiation on the presence and evolution of cloud water. Aircraft measurements and photogra-

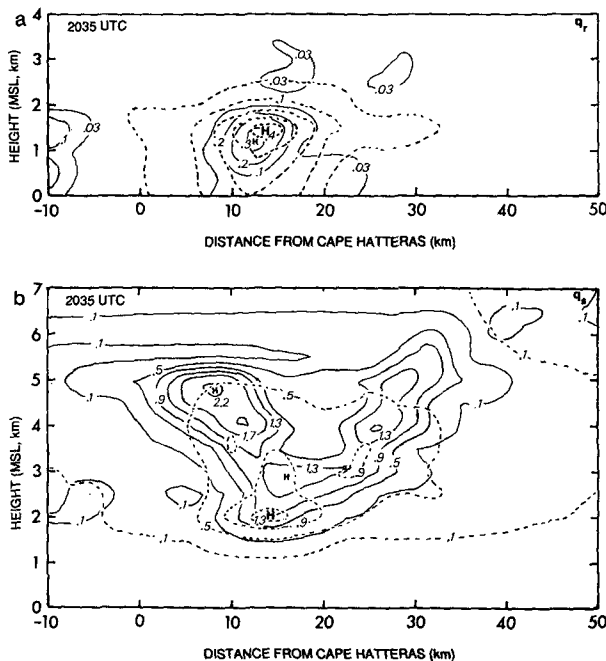


FIG. 7. Vertical cross section across the width of R2 (within the hatched rectangle shown in Fig. 3) of the combined TMR results at 2035 UTC March 6 1986 (solid line) for the mixing ratio (in  $\text{g kg}^{-1}$ ) of a) rain, and b) snow. The mixing ratios derived from measured radar reflectivities (dashed lines) are also shown.

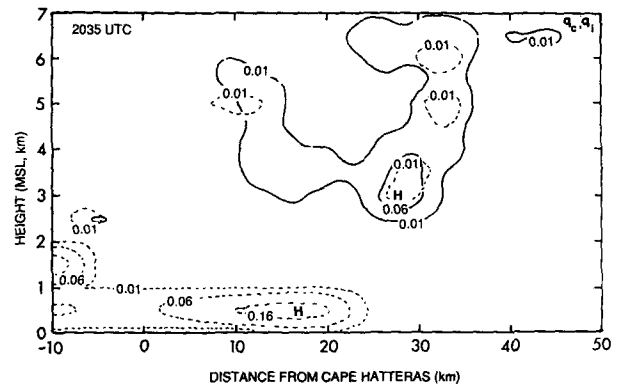


FIG. 8. Combined TMR results for the mixing ratio of cloud water (dashed lines) and cloud ice (solid lines) in a vertical cross section across the width of R2 (within the hatched rectangle shown in Fig. 3) at 2035 UTC March 6 1986.

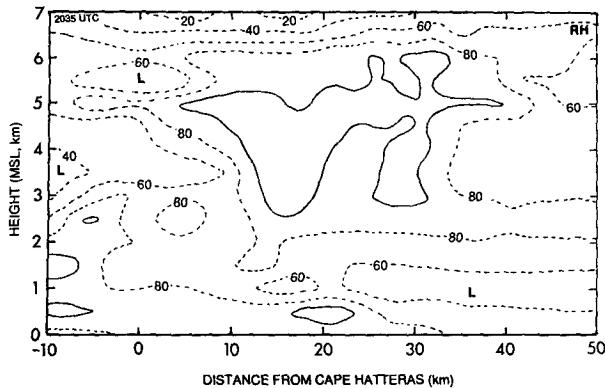


FIG. 9. As for Fig. 8 but for RH (in %) with respect to water. The solid contour is 99%. The symbol "L" is used here (and in following figures) to indicate local minima.

phy indicate that the retrieved amounts and areal extent of both cloud ice and cloud water may be too small. This is due in part to the dryness at upper levels, which is related to the imposed vertical velocity restraint at the top. In fact, the cloud top of R2 was around 8 km, but no velocity data are available above 7 km.

In the cross section of R2 discussed in this study, there is no secondary radar reflectivity maximum in the lower rear region of the rainband associated with the precipitating cumulus observed there. However, just to the SSW of this section cumulus clouds seem to be present (Fig. 3), and the velocity distribution suggests that such cumuli may be forming (precipitation lags vertical velocity, whereas the model results are equilibrium fields). Indeed, 5 min later, in a cross section following the storm motion, a secondary shallow peak in radar reflectivity developed to the rear of R2 (Fig. 10).

Using the combined TMR results, we calculated water budgets for different segments of R2. The vertical flux of water vapor is shown in Fig. 11a (dotted line). An equivalent precipitation of up to  $2.0 \text{ mm h}^{-1}$  is transported through R2. However, not all of this water vapor was condensed or deposited in the updraft, and of the water vapor that did change phase little reached the ground. The integrated amount of precipitation reaching the ground is 0.9 mm. This compares well to the rainfall collected during the passage of R2 in the closest raingauges, all onshore (1 mm, 0.25 mm and 1.25 mm for PAM 45, 40 and 35, respectively; see also Fig. 6 in Part II). So R2 was not an efficient rain producer. Here, we define the precipitation efficiency (PE) of R2 as the ratio of the precipitation reaching the ground to the amount of water vapor condensed or deposited plus the net horizontal condensate influx<sup>1</sup> into the model domain. From the retrieved TMR re-

sults (Table 1) a PE for R2 of 4.6% is calculated. Table 1 shows that the PE was low mainly because most of the condensate formed snow that subsequently sublimated or evaporated after melting. There was a net horizontal condensate outflux, which was small compared to the amount of water vapor condensed or deposited; this indicates that our model domain encompasses most of the width of R2. Hegg et al. (1989), using a microphysical retrieval model, calculated a PE of 8% for R2 at an earlier time, when more precipitation reached the surface.

It is not surprising, for such a low PE, that the profile of latent heating is negative at low levels (below 3 km) due to evaporation/sublimation, with a maximum cooling at 2 km associated with the melting band. It is generally positive from 3 km upward, with a maximum of  $3^\circ\text{C}$  per hour heating at 5 km. Latent heat (Fig. 12) is released by deposition in and downstream of the two main updrafts (Fig. 6), and heat is released by condensation just ahead of the main rainshaft and close to the rear boundary in shallow precipitating cumulus. Downstream of the rainshaft, cooling by sublimation/evaporation occurs at all levels. Below 3 km the cooling is proportional to the precipitation intensity, which may explain the downdraft (Fig. 6) in the rainshaft.

## 2) THERMODYNAMICS

The equilibrium temperature field is shown in Fig. 13 as a perturbation with respect to the upstream boundary. Both gridwide and small-scale features can be seen. On the larger scale, the temperature perturbation structure reveals a high degree of stratification. This is due in part to the choice of lateral boundary conditions, which impose a front-to-rear gradient that varies in strength with height. This effect is most visible toward the rear of R2. In particular, the temperature distribution reveals three boundary-related colder areas to the rear, one at 3 to 3.5 km altitude, one close to the top, and one at the surface. The first one is associated with the midlevel rear-to-front intrusion (Figs. 5 and 9). The higher zonal temperature gradients at upper levels in the cross section are largely in accordance with thermal wind balance. The region to the rear and close to the surface is cooled by melting and evaporation in the main downdraft.

The stratification is also related to the method of combined TMR. In a purely microphysical retrieval, temperature perturbations are much more sensitive to the local vertical air velocity. In combined TMR, on the other hand, the gridwide vertical velocity is important [see (17)]. Therefore, a strong vertical velocity core can have distant effect. Also, a microphysically retrieved temperature profile is not necessarily dynamically balanced; in TMR, temperature is constrained to a dynamical balance, mainly a momentum balance (see section 3c). As such, the impact of phase changes (Fig. 12) on the temperature distribution should be small.

<sup>1</sup> This term is included because there was some horizontal flux of condensate across the rear and front boundaries of the model domain.

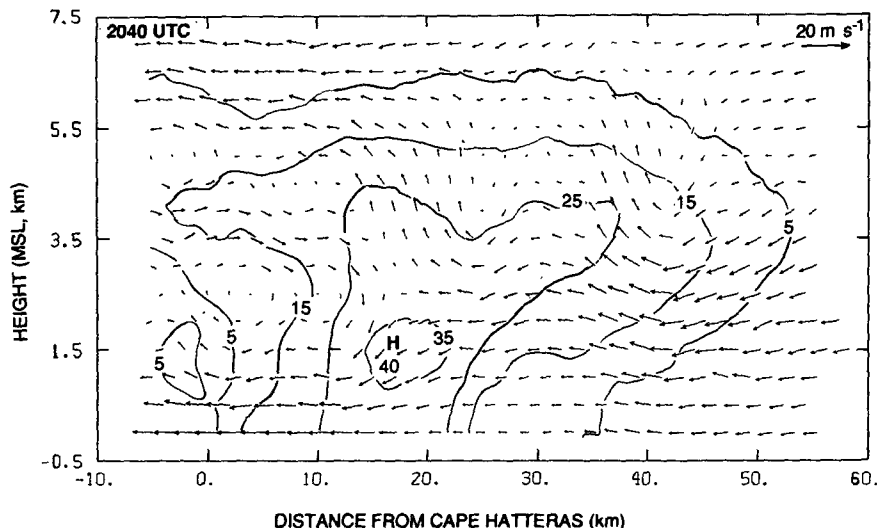


FIG. 10. As for Fig. 5 but at 2040 UTC March 6 1986.

A dominant feature in Fig. 13 is the warm lens around 2–3 km altitude in the middle of the domain. This lens is capped by a cold layer; below the lens, fairly cold air resides just below the freezing level. The lens is located at the base of the updrafts (Fig. 6). The temperature distribution associated with this perturbation, together with the distribution of moisture, is needed to allow for upright or slantwise moist conditionally neutral lifting, as will be shown later. It is of interest to note that in the temperature perturbation distribution shown in Fig. 13 there are no nonhorizontal frontal surfaces.

The resulting equivalent potential temperature ( $\theta_e$ ) distribution is shown in Fig. 14. Since none of the calculations have proceeded along streamlines, internal consistency can be checked through trajectory analysis of conserved variables. Only mixing and melting can change  $\theta_e$  of a parcel. A better measure would be the ice-liquid water potential temperature ( $\theta_{ie}$ ), which is designed to account for the effect of melting (Hauf and Holler 1987). Although in an inviscid environment  $\theta_{ie}$  is not strictly conserved when ice is produced or lost below 0°C, it is conserved better than  $\theta_e$ . For example, along streamlines entering R2 from the PBL ahead of R2,  $\theta_e$  increases by  $\sim 4^\circ\text{C}$  during lifting from 1.5 to 2.5 km, whereas,  $\theta_{ie}$  increases by only  $\sim 2^\circ\text{C}$ . A similar effect of the exclusion of the ice phase was reported by Ziegler (1988).

At the upper levels,  $\theta_e$  varies only slightly across the domain; the slight decrease of  $\theta_e$  is due to the weak front-to-rear cooling (Fig. 13). The upstream boundary is essentially stable at all levels, especially from 1 to 2.5 km, above the top of the dry PBL (Fig. 9). The stratification in this layer (1 to 2.5 km) disappears with the passage of R2, due to downward transport of higher  $\theta_e$  air in the main downdraft, which is moistened by

evaporating rain. The area of the main rainshaft, between  $x = 10$  km and  $x = 15$  km, is almost neutral to convective instability. The shallow precipitating cumulus to the rear is locally convectively unstable.

Most conspicuous in Fig. 14 is the low  $\theta_e$  air coincident with the mid-level rear-to-front intrusion (Fig. 5); it is characterized more by a moisture deficit than by a temperature deficit. This intrusion penetrates into the main rainshaft of R2, then largely subsides along the streamlines (around  $x = 10$  to  $x = 15$  km), returning in an area of evaporating precipitation. This modifies the boundary layer structure across R2, changing the humidity in the PBL more than the momentum and temperature. The subsidence of the low- $\theta_e$  intrusion in the rainshaft is important because it breaks up the dry and convectively stable PBL. The return flow of moist air, with an increased  $\theta_e$  produced by mixing with air close to the surface, is convectively unstable under the midlevel low  $\theta_e$  intrusion; the ensuing cumulus convection, with tops no colder than  $-7^\circ\text{C}$  (Fig. 13), is glaciated (Fig. 7b, Fig. 8) and some precipitation reaches the ground (Fig. 7a).

There is reasonable similarity between the retrieved  $\theta_e$  distribution (Fig. 14) and that derived from aircraft and sounding data (Fig. 8a in Part II; Fig. 15 in Part I). In particular, both cross sections have in common a minimum in  $\theta_e$  at the lower leading edge of R2 and at midlevels to the rear of R2. The leading edge of the midlevel intrusion of low  $\theta_e$ , which we identified in Part II as the leading edge of a weak cold front aloft (CFA), is shown by the thick dashed line in Fig. 14. The retrieved fields presented here corroborate the interpretation of the low-level stable airmass ahead of R2 and the penetrating midlevel wedge to its rear as constituents of an elevated frontal structure. Even though this frontal structure was very weak and poorly

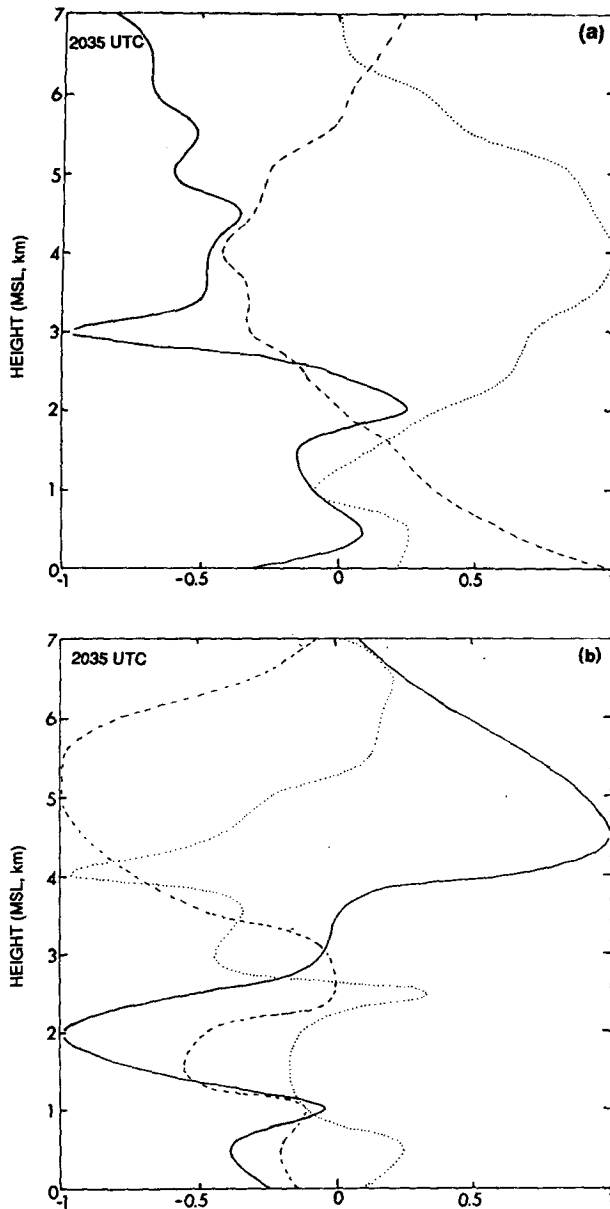


FIG. 11. Height profiles of thermodynamic variables in R2 derived from the combined TMR results. The variables are normalized by their extreme value. An upward flux is defined as positive. (a) Solid line: buoyancy force with respect to the right hand boundary of the cross section (extreme value:  $-0.046 \text{ m s}^{-2}$ ). Dashed line: kinetic energy change (extreme value:  $0.027 \text{ W m}^{-3}$ ). Dotted line: vertical flux of water vapor (maximum value corresponds to a local equilibrium precipitation intensity of  $2.0 \text{ mm h}^{-1}$ ). (b) Solid line: vertical flux of along-band momentum (extreme value:  $0.36 \text{ m}^2 \text{ s}^{-2}$ ). Dashed line: vertical flux of perturbation pressure (extreme value:  $-5.9 \text{ Pa m s}^{-1}$ ). Dotted line: vertical flux of buoyancy (extreme value:  $-0.27 \text{ } 10^{-3} \text{ m s}^{-1}$ ).

defined on the meso- $\beta$  scale, it was vital for the maintenance of R2. As R2 moved farther offshore, the convection behind it developed to greater heights, as it was fed by moist BL air over the Gulf Stream waters and

TABLE 1. Components of the water balance for the model domain of R2 (the hatched region in Fig. 3) calculated from the combined TMR results. Units are in  $10^5 \text{ kg s}^{-1}$ .

|  |       |
|--|-------|
| Evaporation of rain and cloud water                          | 23.3  |
| Sublimation of snow and cloud ice                            | 40.3  |
| Condensation of water vapor on rain and cloud water ( $C$ )  | 7.5   |
| Deposition of water vapor on snow and cloud ice ( $D$ )      | 65.3  |
| Net horizontal condensate influx ( $I_c$ )                   | -2.3  |
| Net horizontal water vapor influx                            | 5.5   |
| Precipitation ( $P$ )  | 3.3   |
| Precipitation efficiency $PE \equiv \frac{P}{(C + D) + I_c}$ | 0.046 |

by the upper PBL moistened by precipitation falling from R2. Eventually, about 2 h after the period for which retrievals are shown here, the convection penetrated to the tropopause (rainband R3 in Part II), which caused R2 to collapse [see Part II, and also Hobbs (1987)]. In fact, the retrieved  $\theta_e$  at the nose of the frontal intrusion is already frontolytic at the time of our analysis, because the frontolytic effect of a convectively stable stratification (Fig. 14) at a frontal boundary, which separates updrafts from downdrafts (Fig. 6), dominates the frontogenic effect of horizontal convergence across the CFA (Sanders 1955).

The retrieved buoyancy field with respect to the mean buoyancy at each horizontal level is shown in Fig. 15. Because the mean buoyancy varies with height with respect to the upstream boundary, its profile is shown in Fig. 11a (solid line). This profile shows that below a height of 3 km, the passage of R2 did not affect the buoyancy very much. At middle and upper levels, the upstream air is buoyant with respect to R2. On a more local and dynamically relevant scale, a positively buoyant layer exists at the base of the midlevel updrafts described in section 4b. This buoyancy is due mainly to temperature excess (Fig. 13). Precipitation loading may contribute to a negative buoyancy in some places,

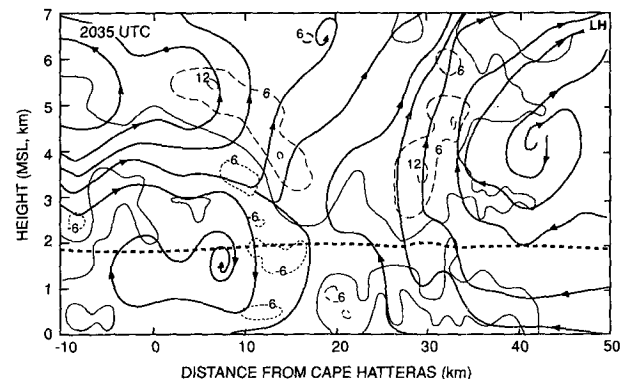


FIG. 12. As for Fig. 8 but for latent heating (in  $^{\circ}\text{C h}^{-1}$ ). Dashed and dotted contours indicate heating and cooling, respectively. The thin solid lines separate regions of net heating from regions of net cooling. The heavy dotted line is the freezing level. Some streamlines (heavier solid lines with arrows) are also shown.

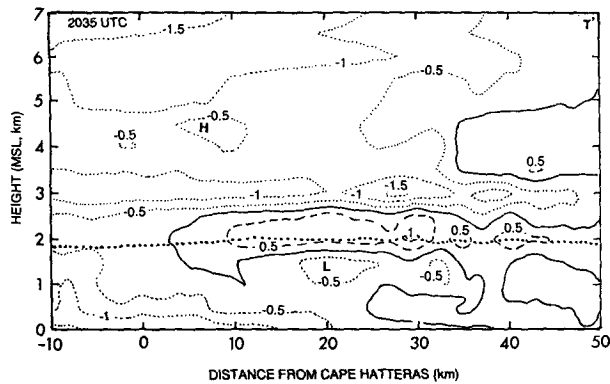


FIG. 13. As for Fig. 8 but for temperature perturbation (in °C) with respect to the right hand boundary of the cross section. Dashed lines contour positive values, dotted lines contour negative values, and the line of zero temperature perturbation is solid. The heavy dotted line is the freezing level.

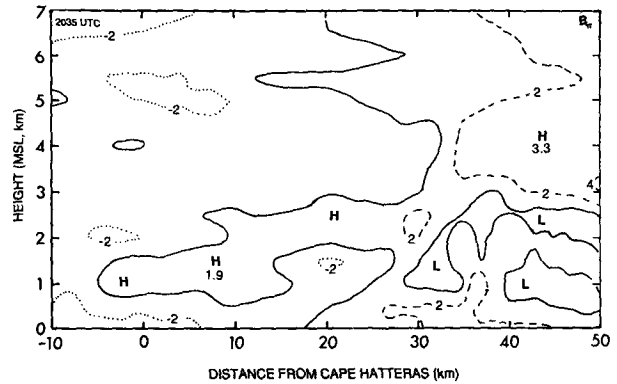


FIG. 15. As for Fig. 8 but for the buoyancy force (in units of  $10^{-2} \text{ m s}^{-2}$ ). The layer-average buoyancy is zero. Dashed lines contour positive values, dotted lines contour negative values, and the line of zero buoyancy is solid.

for instance in the secondary updraft (at  $x = 10 \text{ km}$ ,  $z = 5 \text{ km}$  in Fig. 6), but usually it is insignificant.

Because the retrieved buoyancy depends on all of the equations of motion, its validity can be evaluated by checking the balance of the original equations. A normalized root-mean-square error,  $E_{rb}$ , can be calculated for the cross section based on Eqs. (14)–(15), in the same way as the momentum checking parameter for pressure,  $E_{rp}$  (Gal-Chen and Hane 1981), is derived from Eqs. (6)–(7). Since buoyancy depends on both momentum conservation and the thermodynamic equations and since it is very sensitive to errors in vertical velocity, we expect buoyancy to be retrieved less accurately than pressure (e.g., Lin et al. 1986; Hauser et al. 1988). For the model run described here, we found a value for the relative error  $E_{rb}$  of 0.37. As shown by Gal-Chen and Kropfli (1984), if the buoyancy field carries little small-scale information, the relative error  $E_{rb}$ , which checks the overall accuracy of (1), (2) and (8), should be less than 0.5. However, Hane and Ray

(1985) pointed out that retrieved fields still contain much relevant information, even if the value of  $E_{rp}$  (or  $E_{rb}$ ) is close to unity.

### 3) DYNAMICS

The retrieved pressure perturbation field with respect to the eastern boundary is shown in Fig. 16. The choice of Dirichlet-type boundary conditions for (19) removes the problem of vertical continuity of pressure perturbations derived on a horizontal plane (e.g., Roux 1985; Parsons et al. 1987). Following the technique of Gal-Chen and Hane (1981), we calculated the momentum checking parameter  $E_{rp}$  based on (6) and (7). For various runs we obtained values for  $E_{rp}$  between 0.30 and 0.35, which is significantly less than the 0.5 critical value obtained from random output (Gal-Chen and Kropfli 1984).

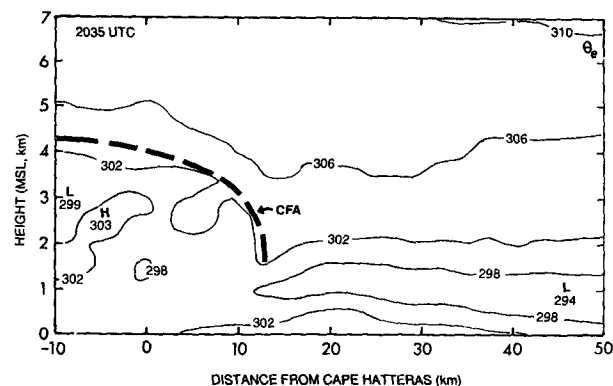


FIG. 14. As for Fig. 8 but for equivalent potential temperature  $\theta_e$  (in K). The thick dashed line delineates the leading edge of the cold front aloft.

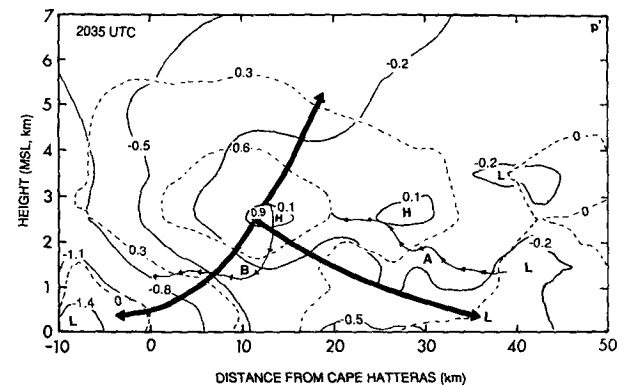


FIG. 16. As for Fig. 8 but for the pressure perturbation (in mb) with respect to the right hand boundary of the cross section. Solid lines contour the total perturbation and dashed lines the ageostrophic part. The thick arrows show the direction of the non-hydrostatic ageostrophic pressure gradient force. The thin arrowed lines, labeled A and B, show the two air trajectories discussed in the text.

At all levels, except from about 2 to 4 km, the pressure drops fairly homogeneously across R2, by about 1 mb from front to rear (Fig. 16), in association with the strong along-band flow. At midlevels, a local region of high pressure is present at the nose of the penetrating CFA (Fig. 14). An inspection of Fig. 15 shows that at least some of the pressure is hydrostatically balanced, for example, the low pressure at the surface just ahead of the rainshaft ( $x = 20$  km to  $x = 30$  km). Except for this local high, a large part of the horizontal pressure perturbation gradient force opposes the eastward Coriolis force. Removal of this part of the pressure perturbations leads to the ageostrophic pressure perturbations (shown as the dashed lines in Fig. 16); its gradient (indicated by the thick arrowed lines in Fig. 16) gives the direction of the vertical and horizontal acceleration in the absence of buoyancy (and subgrid-scale dissipation). Because of the arbitrariness of the mean state from which the perturbations are derived, the pressure gradient field extracted from Fig. 16 is more valuable than the pressure field itself, and it contains all the dynamically relevant information for pressure. In terms of ageostrophy, the leading edge of the rear-to-front intrusion coincides with a high-pressure core, with forcing both up and downward. The downward forcings (both forward and backward, Fig. 16) are stronger because of a low-pressure center in the lower regions to the front and rear. The midlevel rear-to-front intrusion penetrates against the pressure gradient.

To further examine the dynamical structure of R2, we investigated energy conservation along streamlines, based on the steady-state assumption in the combined TMR model. Application of the energy balance equation (e.g., Parsons et al. 1987) along streamlines is complicated by the inhomogeneity of density and buoyancy along the path, and by the motion of the storm. We verified that ignoring friction is valid at midlevels. With this assumption and the energy equation derived from (1) and (2) in a storm-relative frame, it can be shown that the following quantity is conserved between any two points along a trajectory:

$$\Delta \left( \frac{u^2 + v^2}{2} \right) + \Delta \left( \frac{p'}{\rho_b} \right) + f \left( V \Delta x - \int \frac{v}{u} U dx \right) - g \int B_\tau dz - \frac{1}{H} \int \frac{p'}{\rho_b} dz \quad (20)$$

I

II

III

IV

V

where  $\Delta$  is the difference in the values of a parameter between the two points,  $\Delta x$  the horizontal distance between the points, and  $H$  the anelastic scale height. Terms I and II in (20) are the storm-relative kinetic energy and the perturbation pressure potential energy, respectively; they correspond to the Bernoulli equation

TABLE 2. Energy balance along the air trajectories A and B indicated in Fig 16. Units are  $\text{m}^2 \text{s}^{-2}$ .

| Trajectory | Value of terms in Eq. (20) |     |     |     |    | Imbalance |
|------------|----------------------------|-----|-----|-----|----|-----------|
|            | I                          | II  | III | IV  | V  |           |
| A          | -44                        | 71  | -35 | -10 | -4 | -22       |
| B          | 29                         | -73 | -9  | 18  | 10 | -25       |

for an incompressible, adiabatic, steady Galilean system. Term III in (20) vanishes if the storm is stationary, term IV involves buoyancy potential energy, and the last term arises from compressibility. The first two terms in (20) are usually dominant, but the other terms may be equally important, depending on the storm motion and the slope and length of the trajectory.

Table 2 shows the result for a trajectory entering the high pressure area (A in Fig. 16) and for one leaving this area (B in Fig. 16). In both cases, the change in kinetic energy opposes the change in potential energy, but the last two terms—mainly the buoyancy potential energy—act in the same direction, and serve to counterbalance the perturbation pressure potential energy. In view of the assumptions we have made, the magnitudes of the imbalances in Table 2 indicate reasonable internal consistency.

The dynamical structure of R2 can be elucidated further by analyzing the distribution of pressure and buoyancy in terms of a force balance. A combination of weak vertical shear of the horizontal wind (Fig. 4b) and weak vertical velocity gradient (Fig. 6), makes the effect of sheared updrafts on the pressure distribution quite small (Rotunno and Klemp 1982; Lemone et al. 1988). In the absence of strong updrafts, strong shear, and strong wind, it follows from (19) that positive (negative) vertical pressure perturbation gradients (Fig. 16) and positive (negative) buoyancy (Fig. 15) are often collocated. In the present case, this is true for 75% of the grid points, and the linear regression coefficient between buoyancy and pressure perturbation gradient force is  $-0.85$ .

From the aspect ratio (height/length) of R2 it follows that the horizontal derivative in the 2-D Laplacian on the lhs of (19) is two orders of magnitude smaller than the vertical derivative; so, to a first approximation, the horizontal derivative in the 2-D Laplacian of (19) can be neglected. Then, in the absence of strong updrafts, strong shears and strong winds, (19) reduces to (7) with  $\Gamma = 0$  in an incompressible, adiabatic atmosphere with an unperturbed reference level. This implies that to a large extent the *perturbations* are hydrostatic (Gordon 1981). This is not surprising, given the aspect ratio of R2 and the magnitude of the updrafts. In fact, the microphysical and thermodynamic fields retrieved from a hydrostatic model [in which  $\Gamma$  is set to zero in (7)] are quite similar to those shown in the present

study. On more local scales (e.g., on the order of the two updrafts in Fig. 6), the hydrostatic approximation is not very accurate.

The strongest updraft core that was measured in R2 [at  $(-32, 4)$  in Fig. 6] was maintained by a positively buoyant layer below (from 2 to 2.5 km height in Fig. 15). On its upstream side, this buoyant layer is surrounded by a hint of a dipole structure in pressure between 3 km and the ground (Fig. 16). This consists of a downward pressure perturbation force through the buoyant layer, and a weaker curvilinear force upstream of the buoyant core.<sup>2</sup>

#### d. Verification

The internal consistency checks discussed in section 4c show how well the resulting fields satisfy the equations with which we started; the presence of a field that closely obeys two dynamical constraints gives confidence about its reality, or at least about its accuracy, given the input flow field and boundary conditions, and our system of equations, parameterizations and assumptions. We will now check some of the combined TMR model outputs by comparing them with independent measurements. In doing so, we cannot eliminate the spatial and temporal discrepancy that may exist between the measurements and the model. The verification will also test the two main assumptions that we made in our combined TMR model: two-dimensionality and steady-state flow. With the across-band variation seen in Fig. 3, boundary fluxes of water and heat may exist that make the predetermined lateral boundary conditions effectively insignificant. The along-band flow is quite strong (Fig. 4b), and evolving cloud patterns may be advected into the cross section by the along-band shear (Fig. 4b).

We have two sources of independent verification: radar reflectivity and aircraft observations. To check the distribution of the hydrometeors predicted by the combined TMR, we used the radar and airborne measurements to derive a relationship between radar reflectivity and hydrometeor concentration. Mixing ratios of the hydrometeors were obtained from integrated measurements on flight leg sections with fairly homogeneous radar reflectivities. From this relationship, and the position of the freezing level, the "measured" concentrations of rain and snow were derived. We did not attempt to correct for the effect of the bright band below the freezing level ( $\sim 1.85$  km) (Ziegler 1988),

so snow and rain concentrations are slightly overestimated at that altitude. These concentrations are compared to the model results in Fig. 7. There are considerable discrepancies between "measured" and retrieved snow and rain, but the locations of the peak concentrations predicted by the retrieval model agree fairly well with the measurements. The rain concentration is slightly underestimated in the model, while the model integrated and peak concentrations of snow are larger by 62% and 77%, respectively. This excess snow is mainly at upper levels (4–5 km height) in regions where the updraft (Fig. 6) suspends the snow.

In Fig. 17, we compare the results of various variables from the combined TMR model with measurements obtained on two penetrations of R2 by the University of Washington's C-131A research aircraft. The cloud ice mixing ratio was determined by integrating ice crystal sizes derived from PMS 2-D and 1-D measurements aboard the aircraft. Neither of these two flight legs occurred at the exact time and place of the combined TMR model results presented here. However, the flight leg from the rear to the front of R2 (Fig. 17a, with distance inverted) occurred about 0.5 h later and in storm-relative coordinates about 40 km to the SSW of the southern edge of the retrieval area in Fig. 3. The front-to-rear aircraft leg (Fig. 17b) took place about 1 h earlier and about 150 km to the NNE of the northern edge of the retrieval area.

The variables compared in Fig. 17 generally show reasonable agreement. However, the model predicts the heaviest snowfall to be located about 10 km to the rear of where it was observed from the aircraft, and the retrieved snow concentrations are generally less than measured (Fig. 17a). The airborne measurements confirm the presence of ice (but in larger amounts than in the retrieval) in the trailing shallow precipitating cumulus (Fig. 8), even though the temperature is only just below freezing (Fig. 17a). The model did not reproduce the liquid water observed from the aircraft in the upstream inflow of R2. In fact, the model underestimates the RH in this region by over 10%. Another significant difference between the TMR model results and the measurements is the large amplitude oscillation in  $\theta_e$ , reflected in the RH trace. This perturbation is associated with the downward extension of the penetrating cold front aloft (around  $x = 10$  km), which was preceded by a high- $\theta_e$  rain shaft (around  $x = 15$  km). This oscillation is hardly discernible in the airborne measurements, either at 2105 UTC (Fig. 17a) or 1925 UTC (Fig. 17b), indicating that these flight legs were situated below the CFA. The retrieved temperature trace agrees well with the measurements on the larger scale features, except for a 0.5 to 1°C underestimate at 2100 UTC (Figs. 17a and 17b). The retrieved low- $\theta_e$  lower level, front-to-rear inflow suggested by the MRH 1800 UTC sounding (Fig. 4a) penetrates further into R2 and is more pronounced than that measured in the 1930 UTC flight leg (Fig. 17b).

<sup>2</sup> An analogy with electrostatics may be useful here. Let  $\pi'$  correspond to electric potential,  $\nabla\pi'$  to electric field, and  $-(\partial\rho'/\partial z)$  (the vertical buoyancy gradient) to charge density. Then (22) without the second term is equivalent to the Poisson equation in electrostatics. Hence, for any charge (buoyancy) distribution, the direction of the electric field corresponds to the direction of the pressure gradient force. This analogy can be used to visualize buoyancy-induced pressure perturbation patterns around buoyant cells.

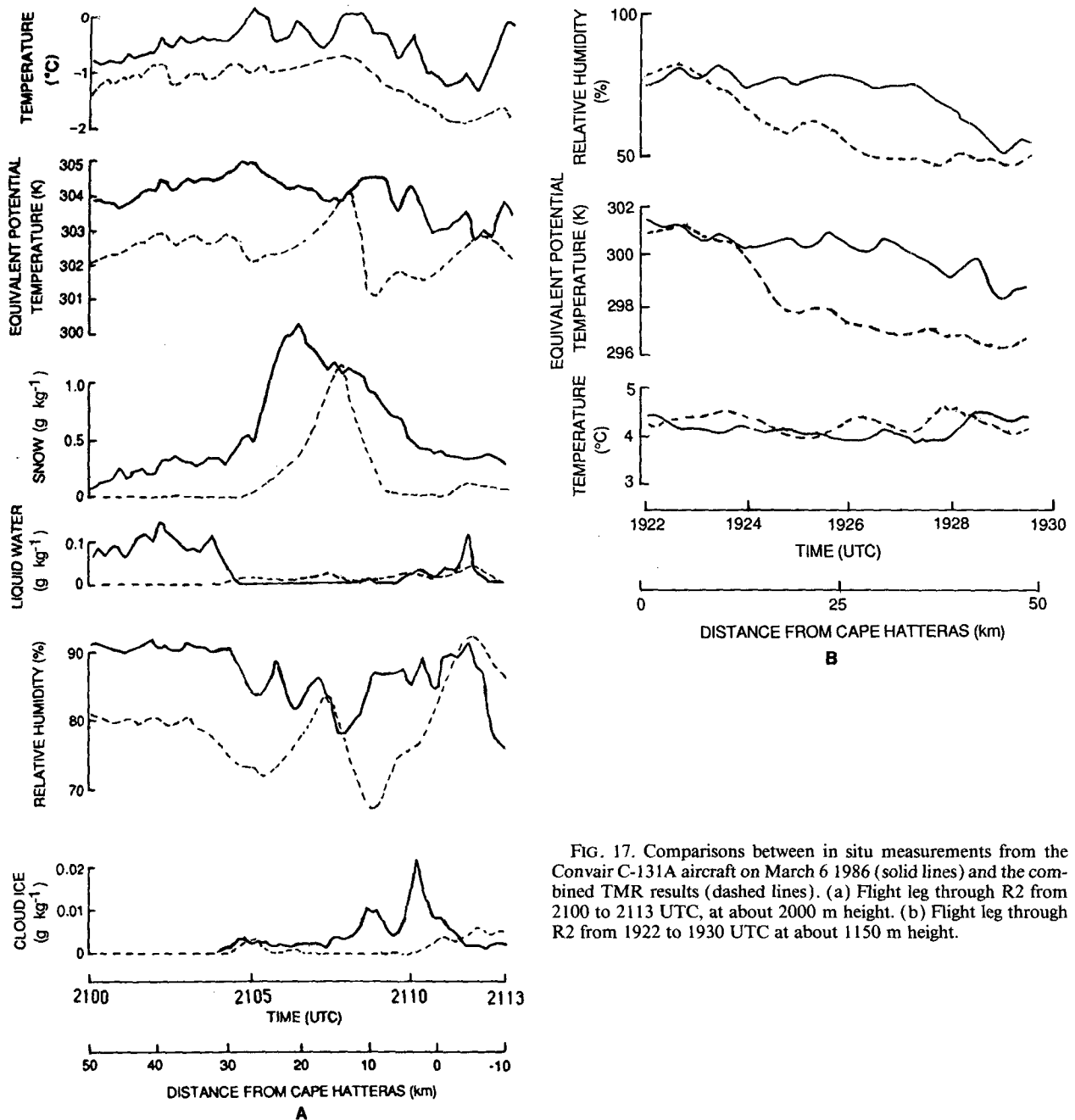


FIG. 17. Comparisons between in situ measurements from the Convair C-131A aircraft on March 6 1986 (solid lines) and the combined TMR results (dashed lines). (a) Flight leg through R2 from 2100 to 2113 UTC, at about 2000 m height. (b) Flight leg through R2 from 1922 to 1930 UTC at about 1150 m height.

### e. Discussion

In Part II we classified R2 as a wide cold-frontal rainband, since it was situated at the leading edge of relatively dry, cold air associated with a cold front that was detached from the PBL. Martin et al. (1990) and Hobbs et al. (1990) refer to the latter as a cold front aloft (CFA). The air mass behind the CFA was characterized more by a moisture deficit than by a temperature deficit, most likely because the air had descended over the continent (see Part I). The midlevel

forcing associated with the CFA lifted air that was originally stable (Fig. 4a). This lifting made the air weakly unstable; hence, the front was instrumental in maintaining R2 (see section 4c).

The question arises as to whether conditional symmetric instability (CSI) was essential for the maintenance of R2 (Bennets and Hoskins 1979; Parsons and Hobbs 1983). The orientation of R2, which was close to the wind shear (Fig. 4b), is consistent with CSI [this allows us to compare the moist isentropic potential vorticity distribution to the isolines of absolute pseudo-

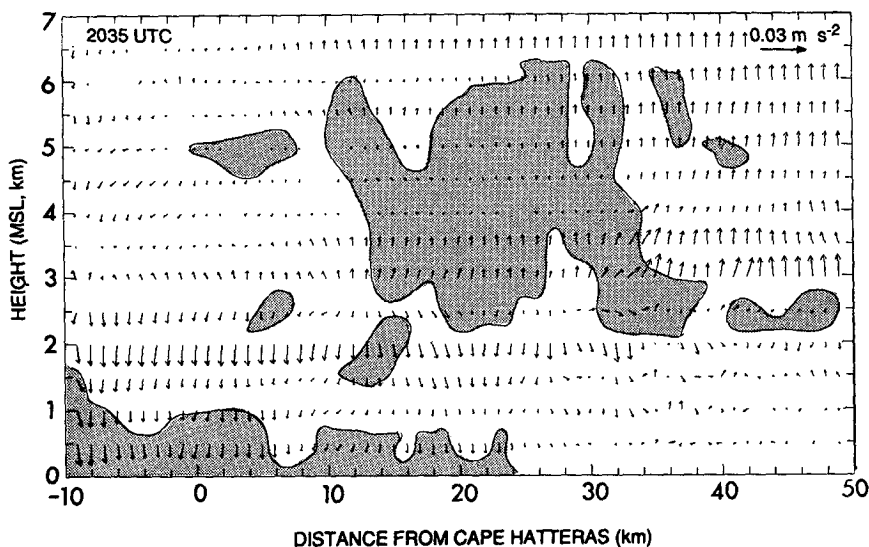


FIG. 18. As for Fig. 8 but showing, by means of vectors, the Langrangian acceleration that parcels of air experience. The shaded region has a RH  $\geq$  85% with respect to water and is neutral or unstable with respect to CSI.

angular momentum (M-surfaces, Emanuel 1983) and isentropes in the cross section]. However, orientation is not a sufficient condition for CSI to be effectively functional. In fact, R2 was parallel along its entire length to the trailing surface front (Part II, Fig. 2). Figure 18 shows that CSI (and *not* convective instability, Fig. 14) was present in the saturated air ( $\geq$ 85% RH with respect to water) in an extensive region ahead of the nose of the intruding CFA, a region that encompasses the two main updrafts (Fig. 6). As such, CSI was responsible for the fairly deep convection seen in the aerial photography (Fig. 10 in Part II) and radar imagery. Some CSI (and convective instability) was also present in the boundary layer below and behind R2, and in the trailing shallow precipitating cumulus.

The orientation, position, width and duration of R2 were controlled by a larger scale circulation, in which both frontogenesis and CSI were important. Locally, the midlevel convergence made the air unstable to slantwise convection (Fig. 5). This slantwise convection drove the circulation of R2; this convection was also an essential ingredient in the meso- $\alpha$  circulation, of which the midlevel, rear-to-front intrusion was a component. Larger scale analysis (see Parts I and II) indicated that the latter circulation was frontal and that it had a long history. If local instantaneous (slantwise) instability were the sole engine of R2, one would expect to see more upward acceleration of the air in the region where the moist isentropic potential vorticity is negative, rather than in a larger region ahead of the CFA (Fig. 18). The retrieval results indicate that the air was accelerated upward ahead of the CFA, and that the vertical motion was suppressed below this region.

To further examine this issue, we computed the pro-

file of kinetic energy change as an air parcel moves through R2 in a fixed frame of reference (the dashed line in Fig. 11a). The profile shows that parcels are accelerated below 2 km and decelerated at midlevels. The low-level acceleration along the air trajectories is a downgradient acceleration that opposes friction. The midlevel deceleration is due to the convergence along the CFA: the energy released is used in the momentum exchange with the PBL, in the cooling of the middle and upper levels (Fig. 13), and to build up the (ageostrophic) pressure differences (Fig. 16) that are needed to maintain the entire circulation associated with R2. Therefore, external forcing was needed to maintain R2. It can be shown from (1) and (2) that in the absence of friction the horizontal average of the kinetic energy change is given by

$$\frac{\rho_b dE_{kb}}{dt} = \frac{p'u(l)}{L} - \frac{1}{\rho_b} \frac{\partial \rho_b(p'w)_b}{\partial z} + g(Bw)_b \quad (21)$$

where  $E_{kb}$  is the 3-D kinetic energy,  $L$  the horizontal length of the grid, and the subscript b refers to horizontal averaging. The first term on the rhs of (21) is evaluated at the rear boundary of R2. The second term is the energy flux convergence of an internal gravity wave. As shown in Fig. 11b (dashed line), this flux converges between 3 and 5 km and diverges from 2 to 3 km and also below the cloud top. The convergence of wave energy into midlevels (3–5 km) opposes the loss of kinetic energy. This loss is mainly due to the negative vertical flux of buoyancy (Fig. 15); this negative flux, the third term in (22), is a transfer from kinetic to potential energy (Fig. 11b, dotted line). The lifting cools the middle and upper levels of R2. The

effect on upper levels is smaller, in part because of the suppressed vertical velocity aloft (see section 2).

To demonstrate that frontal energy—or, more generally, energy derived from a larger scale than that of the rainband itself—supported the circulation of R2, we computed the vertical flux of wind along R2, which is basically vertical flux of the large-scale wind (Fig. 4b). Vertical convergence of this flux accelerates the large-scale wind, which, through thermal wind balance, is a good measure of the large-scale energy. As can be seen in Fig. 11b (solid line), this flux is divergent between 2 and 4.5 km. This corresponds to the altitude of penetration of the low- $\theta_e$  wedge (Figs. 5 and 14). Hence, the large-scale flow associated with the trailing CFA provided the energy necessary to maintain R2.

## 5. Conclusions

In this paper we have demonstrated the utility of combined thermodynamic and microphysical retrieval (combined TMR), based on Doppler radar measurements and parameterized cloud microphysics, in analyzing the dynamics of a weakly convective rainband (R2).

Our principal conclusions are:

- The viability of the combined TMR technique has been demonstrated with internal consistency checks and by comparisons with independent measurements. The technique can be used for detailed analysis of the dynamics of observed flow fields and quantitative information can be obtained on the origin and maintenance of even rather weak ( $w < 2 \text{ m s}^{-1}$ ) mesoscale precipitating systems.

- The airflow and retrieved thermodynamic structure of R2 indicated that the rainband was driven by a cold front aloft (CFA). On the scale of the rainband, the CFA exhibited itself as a penetration of cold, dry air into the mid-levels of R2. The combined TMR results indicate that this penetrating wedge interacted with the PBL, not only through moistening by hydrometeors, but also through a shallow downdraft produced by precipitation from R2. Hence, the CFA and R2 were necessary ingredients in the imminent destabilization of the trailing PBL and the development of deep convection to the rear of R2 as the band moved out over the Gulf Stream. This deep convection cut R2 off from the CFA and caused its subsequent demise.

- The lifting of pre-frontal air by the midlevel intrusion made this air conditionally symmetrically unstable. Therefore, some midlevel slantwise convection was present, which interacted with the CFA in the maintenance of the larger scale circulation.

- Overall, R2 was close to hydrostatic balance.

- R2 was quite homogeneous along its length and in steady state during the period ( $\sim 1 \text{ h}$ ) for which we applied the combined TMR. However, both small-scale and large-scale phenomena were observed that were attributed to along-band variation and to transience.

- R2 was an inefficient rain producer (precipitation efficiency  $\sim 5\%$ ). Most of the hydrometeors evaporated, either in the dry PBL ahead of R2 or in the downdraft associated with the intruding CFA.

*Acknowledgments.* Thanks are due to all those who participated in GALE, particularly the NCAR personnel (led by Paul Herzegh) who collected the Doppler radar data. We are also grateful to Owen Hertzman, John Locatelli and Brian Mapes, for very useful discussions and help. Computation was provided by the NCAR, which is supported by NSF. This research was funded by a series of grants from the Atmospheric Research Section of the NSF, the latest of which is ATM-8809061.

## REFERENCES

- Beard, K. T., and H. T. Ochs, 1984: Collection and coalescence efficiencies for accretion. *J. Geophys. Res.*, **89**, 7165–7169.
- Bennets, D. A., and B. J. Hoskins, 1979: Conditional symmetric instability—a possible explanation for frontal rainbands. *Quart. J. Roy. Meteor. Soc.*, **105**, 945–962.
- Brandes, E. A., 1984: Relationships between radar derived thermodynamic variables and tornadogenesis. *Mon. Wea. Rev.*, **112**, 1033–1052.
- Chong, M., and D. Hauser, 1989: A tropical squall line observed during the COPT81 experiment in West Africa. Part II: water budget. *Mon. Wea. Rev.*, **117**, 728–744.
- Emanuel, K. A., 1983: The Lagrangian parcel dynamics of moist symmetric instability. *J. Atmos. Sci.*, **40**, 2368–2376.
- Genesis of Atlantic Lows Experiment (GALE), 1985: *Experiment Design, 1985*, NCAR, 199 pp. [Available from the GALE Project Office, NCAR, Boulder, Co, 80307.]
- Gal-Chen, T., 1978: A method for the initialization of the anelastic equations: implications for matching models with observations. *Mon. Wea. Rev.*, **106**, 586–606.
- , 1982: Errors in fixed and moving frames of reference: applications for conventional and Doppler radar analysis. *J. Atmos. Sci.*, **39**, 2279–2300.
- , and C. E. Hane, 1981: Retrieving buoyancy and pressure fluctuations from Doppler radar observations: A status report. *Atmos. Tech.*, **13**, 98–104.
- , and R. A. Kropfli, 1984: Buoyancy and pressure perturbations derived from dual-Doppler radar observations of the PBL: applications for matching models with observations. *J. Atmos. Sci.*, **41**, 3007–3020.
- Geerts, B., 1990: Retrieval of pressure, temperature, and cloud structure in frontal rainbands. Ph.D. dissertation, University of Washington, 220 pp.
- Gordon, N. D., 1981: Comments on “A three-dimensional numerical model of an isolated thunderstorm. Part II: Dynamics of updraft splitting and mesovortex evolution.” *J. Atmos. Sci.*, **38**, 1798.
- Hane, C. E., and B. C. Scott, 1978: Temperature and pressure perturbations within convective clouds derived from detailed air motions: preliminary testings. *Mon. Wea. Rev.*, **106**, 654–661.
- , and P. S. Ray, 1985: Pressure and buoyancy fields derived from Doppler radar data in a tornadic thunderstorm. *J. Atmos. Sci.*, **42**, 18–35.
- Hauf, T., and H. Holler, 1987: Entropy and potential temperature. *J. Atmos. Sci.*, **44**, 2887–2901.
- Hauser, D., and P. Amayenc, 1986: Retrieval of cloud water and water vapour contents from Doppler radar data in a tropical squall line. *J. Atmos. Sci.*, **43**, 823–838.
- , F. Roux and P. Amayenc, 1988: Comparison of two methods for the retrieval of thermodynamic and microphysical variables from Doppler radar measurements: application to the case of a tropical squall line. *J. Atmos. Sci.*, **45**, 1285–1303.

- Hegg, D. A., S. A. Rutledge, P. V. Hobbs, M. C. Barth and O. Hertzman, 1989: The chemistry of a rainband. *Quart. J. Roy. Meteor. Soc.*, **115**, 867–886.
- Hobbs, P. V., 1978: Organization and structure of clouds and precipitation on the mesoscale and microscale in cyclonic storms. *Rev. Geophys. Space Phys.*, **16**, 741–755.
- , 1987: The Gulf Stream rainband. *Geophys. Res. Letts.*, **14**, 1142–1145.
- , J. D. Locatelli and J. E. Martin, 1990: Cold fronts aloft and the forecasting of precipitation and severe weather east of the Rocky Mountains. *Wea. Forecasting*, **5**, 613–626.
- Le Cam, M. N., and H. Isaka, 1989: Retrieval of microphysical variables by a diagnostic modeling study: comparison between parameterized and detailed warm microphysics. *Tellus*, **41A**, 338–356.
- Lemone, M. A., G. A. Barnes, J. C. Fankhauser and L. F. Tarleton, 1988: Perturbation pressure fields measured by aircraft around the cloud-base updraft of deep convective clouds. *Mon. Wea. Rev.*, **116**, 313–327.
- Lin, Y. J., R. D. Farley and H. D. Orville, 1983: Bulk parameterization of the snow field in a cloud model. *J. Climate Appl. Meteor.*, **22**, 1065–1092.
- Lin, Y. L., T. C. Wang and J. H. Lin, 1986: Pressure and temperature perturbations within a squall line derived from SESAME dual Doppler data. *J. Atmos. Sci.*, **43**, 2302–2327.
- Locatelli, J. D., J. M. Sienkiewicz and P. V. Hobbs, 1989: Organization and structure of clouds and precipitation on the Mid-Atlantic Coast of the United States of America. Part I: Synoptic evolution of a frontal system from the Rockies to the Atlantic coast. *J. Atmos. Sci.*, **46**, 1327–1348.
- Martin, J. E., J. D. Locatelli and P. V. Hobbs, 1990: Organization and structure of clouds and precipitation on the Mid-Atlantic Coast of the United States of America. Part III: The evolution of a middle-tropospheric cold front. *Mon. Wea. Rev.*, **118**, 195–217.
- Matejka, T. J., 1989: Pressure and buoyancy forces and tendencies in a squall line and their relation to its evolution. Preprint, *24th Conf. on Radar Meteorology*, Tallahassee, FL, Amer. Meteor. Soc. 478–481.
- O'Brien, J. J., 1970: Alternative solutions to the classical vertical velocity problem. *J. Appl. Meteor.*, **9**, 197–203.
- Parsons, D. B., and P. V. Hobbs, 1983: The mesoscale and microscale structure and organization of clouds and precipitation in mid-latitude cyclones. Part XI: Comparisons between theoretical and observational aspects of rainbands. *J. Atmos. Sci.*, **40**, 2377–2397.
- , C. G. Mohr and T. Gal-Chen, 1987: A severe frontal rainband. Part III: Derived thermodynamic structure. *J. Atmos. Sci.*, **44**, 1615–1631.
- Pruppacher, H. R., and J. D. Klett, 1978: *Microphysics of Clouds and Precipitation*. Reidel, 714 pp.
- Rotunno, J., and J. B. Klemp, 1982: The influence of the shear-induced pressure gradient on thunderstorm motion. *Mon. Wea. Rev.*, **110**, 136–151.
- Roux, F., 1985: Retrieval of thermodynamic fields from multiple Doppler radar data using the equations of motion and the thermodynamic equation. *Mon. Wea. Rev.*, **113**, 2142–2157.
- , 1988: The West African squall line observed on 23 June 1981 during COPT 81: Kinematics and thermodynamics of the convective region. *J. Atmos. Sci.*, **45**, 406–426.
- , and D. Hauser, 1989: The kinematic, thermodynamic, and microphysical structure of a narrow cold frontal rainband. Preprint, *24th Conf. on Radar Meteorology*, Tallahassee, FL, Amer. Meteor. Soc. 484–497.
- , J. Testud, M. Payen and B. Pinty, 1984: West African squall line thermodynamic structure retrieved from dual-Doppler radar observations. *J. Atmos. Sci.*, **41**, 3104–3121.
- Rutledge, S. A., and P. V. Hobbs, 1983: The mesoscale and microscale structure and organization of clouds and precipitation in mid-latitude cyclones. Part VIII: A model for the seeder-feeder process in warm frontal rainbands. *J. Atmos. Sci.*, **40**, 1185–1206.
- , and —, 1984: The mesoscale and microscale structure and organization of clouds and precipitation in midlatitude cyclones. Part XII: A diagnostic modeling study of precipitation development in narrow cold-frontal rainbands. *J. Atmos. Sci.*, **41**, 2949–2972.
- Sanders, F., 1955: An investigation of the structure and dynamics of an intense surface frontal zone. *J. Meteor.*, **12**, 542–552.
- Sienkiewicz, J. M., J. D. Locatelli, P. V. Hobbs and B. Geerts, 1989: The organization and structure of clouds and precipitation on the Mid-Atlantic Coast of the United States of America. Part II: The mesoscale and microscale structure of a frontal system. *J. Atmos. Sci.*, **46**, 1349–1364.
- Smagorinski, J., 1963: General circulation experiments with the primitive equations. Part I: the basic experiment. *Mon. Wea. Rev.*, **91**, 99–164.
- Yau, M. K., and M. Jean, 1989: Synoptic aspects and physical processes in the rapidly intensifying cyclone of 6–8 March, 1986. *Atmos. Ocean*, **27**, 59–86.
- Ziegler, C. L., 1984: Retrieval of thermal and microphysical variables in observed convective storms. Ph.D. dissertation, University of Oklahoma, 196 pp.
- , 1985: Retrieval of thermal and microphysical variables in observed convective storms. Part I: Model development and preliminary testing. *J. Atmos. Sci.*, **42**, 1487–1509.
- , 1988: Retrieval of thermal and microphysical variables in observed convective storms. Part II: Sensitivity of cloud processes to variation of the microphysical parameterization. *J. Atmos. Sci.*, **45**, 1072–1090.